A 3D personalized cardiac myocyte aggregate orientation model using MRI data-driven low-rank basis functions

Johanna Stimm, Stefano Buoso, Ezgi Berberoğlu, Sebastian Kozerke, Martin Genet, Christian Stoeck

Medical Image Analysis 71 (2021) 102064

Contents lists available at ScienceDirect

Medical Image Analysis

journal homepage: www.elsevier.com/locate/media

A 3D personalized cardiac myocyte aggregate orientation model using MRI data-driven low-rank basis functions

Johanna Stimm[a], Stefano Buoso[a], Ezgi Berberoğlu[a], Sebastian Kozerke[a], Martin Genet[b,c,d], Christian T. Stoeck[a,*]

[a] Institute for Biomedical Engineering, University and ETH Zurich, Zurich, Switzerland
[b] Laboratoire de Mécanique des Solides, École Polytechnique, Palaiseau, France
[c] M3DISIM team, Inria / Université Paris-Saclay, Palaiseau, France
[d] C.N.R.S./Université Paris-Saclay, Palaiseau, France

ARTICLE INFO

Article history:
Received 17 November 2020
Revised 1 March 2021
Accepted 31 March 2021
Available online 9 April 2021

Keywords:
3D cardiac microstructure
Dimensionality reduction
Data-driven parametric model
Personalized modelling
Proper generalized decomposition
Proper orthogonal decomposition

ABSTRACT

Cardiac myocyte aggregate orientation has a strong impact on cardiac electrophysiology and mechanics. Studying the link between structural characteristics, strain, and stresses over the cardiac cycle and cardiac function requires a full volumetric representation of the microstructure. In this work, we exploit the structural similarity across hearts to extract a low-rank representation of predominant myocyte orientation in the left ventricle from high-resolution magnetic resonance ex-vivo cardiac diffusion tensor imaging (cDTI) in porcine hearts. We compared two reduction methods, Proper Generalized Decomposition combined with Singular Value Decomposition and Proper Orthogonal Decomposition. We demonstrate the existence of a general set of basis functions of aggregated myocyte orientation which defines a data-driven, personalizable, parametric model featuring higher flexibility than existing atlas and rule-based approaches. A more detailed representation of microstructure matching the available patient data can improve the accuracy of personalized computational models. Additionally, we approximate the myocyte orientation of one ex-vivo human heart and demonstrate the feasibility of transferring the basis functions to humans.

1. Introduction

The myocardium is composed of a complex microstructure of branching and interconnecting aggregated myocytes (Streeter et al., 1969; Gilbert et al., 2007) grouped in myolaminae (LeGrice et al., 1997; Gilbert et al., 2007; Lunkenheimer and Niederer, 2012). The predominant alignment of myocyte aggregates follows a double helical structure. This pattern has been found across species and suggests that there is a common ground for myocardial structure (Healy et al., 2011).

The structural aggregation of myocytes, has a significant impact on cardiac function. Electrophysiology is influenced by faster electrical conduction in myocyte direction, active contraction is determined by cardiomyocyte orientation, and the anisotropic passive tissue response depends on microstructure. Studies on cardiac motion revealed a high sensitivity of myocardial strain and stress to myocyte orientation (Nikou et al., 2016b; Bovendeerd et al., 1992; Wang et al., 2016). A realistic, high-fidelity representation of the myocardial structure, taking into account inter-subject variability, is therefore essential to reveal the link between cardiac structure and function. Local variations, not captured by homogeneous rule-based representations based on common features observed from histological studies, have been shown to influence cardiac electro-mechanics simulations (Bovendeerd et al., 1992; Wang et al., 2016; Nikou et al., 2016a; Palit et al., 2015a; Eriksson et al., 2013; Rodríguez-Cantano et al., 2019). Including subject-specific, high-resolution myocyte orientation in biomechanical models enables to reduce cross-fiber contraction and to obtain physiologically realistic cardiac simulations (Sack et al., 2018).

Besides direct mapping of high-resolution ex-vivo data, rule-based aggregated myocyte representations and atlas methods are used to provide a 3D volumetic myocyte aggregate orientation field for biomechanical models.

The most commonly used rule-based approaches approximate local myocyte orientation as function of the transmural distance

* Corresponding author.
E-mail address: stoeck@biomed.ee.ethz.ch (C.T. Stoeck).

https://doi.org/10.1016/j.media.2021.102064

from endocardium and epicardium, where helix angles are prescribed (Beyar and Sideman, 1984; Potse et al., 2006; Karadag et al., 2011). More recently, rule-based methods using harmonic solutions of the Laplace equation with Dirichlet boundary conditions at the endo- and epicardial wall have been proposed to obtain a continuous coordinate system adapted to the heart shape. This approach is combined with functions of transmural depth to define the myocytes distribution (Bayer et al., 2012; Rossi et al., 2014; Wong and Kuhl, 2014; Doste et al., 2019). Nagler et al. (2016) extended such a harmonic myocyte aggregate orientation rule including transmural, circumferential and longitudinal variations taking into account helix and transverse angle. In their work, Nagler et al. (2013) suggested a method adapting the boundary conditions to data, by minimizing a cost function comparing measurements and rule-based microstructure by reduced-order static Unscented Kalman Filtering.

Alternatively, statistical atlas methods and statistics-based structure-shape models (Peyrat et al., 2007; Lombaert et al., 2011; Piuze et al., 2013; Lekadir et al., 2014; Zhang and Wei, 2017; Mojica et al., 2020) based on ex-vivo cardiac magnetic resonance diffusion tensor imaging (cDTI) or on in-vivo cDTI data upon tensor interpolation (Toussaint et al., 2010; 2013) have been proposed. Atlas methods provide a template of aggregated myocyte orientation. Atlas methods are based on the high correlation of left ventricular (LV) shape and aggregated myocyte orientation. The template of aggregated myocyte orientation is personalized by mapping it onto a new shape. However, incorporating additional, patient-specific microstructural information remains challenging. A mapping, combining the atlas and additional input data, is needed.

We propose a data-driven low-rank and personalizable structure model. It provides a more detailed representation than classical rule-based approaches with the possibility of model personalization in contrast to atlas methods. Our approach is derived from high-resolution, ex-vivo porcine cDTI data extracting detailed 3D volumetric information about predominant myocyte orientation. We use a shape-adapted coordinate system to map local data between different LV geometries. We exploit the similarity of microstructure across hearts and extract a low-rank basis characterizing aggregated myocyte orientation. We compare two order reduction methods extracting the predominant structural characteristics: an adapted Proper Generalized Decomposition (PGD) (Chinesta et al., 2014; Genet et al., 2015) combined with a Singular Value Decomposition (SVD) and Proper Orthogonal Decomposition (POD) (Buoso et al., 2019).

The model performance is evaluated, comparing the approximation to the original data. To demonstrate the generalization of the basis functions we apply our data-based low-rank model to test data of healthy hearts and hearts with myocardial infarction. Further, we compare the model to a rule-based model based on Bayer et al. (2012) and a myocyte aggregate orientation atlas. To investigate potential clinical use, the data-based low-rank model was applied to a single human heart to demonstrate its capability.

2. Material and methods

Fig. 1 summarizes the workflow of extracting the reduced-order myocyte orientation model from cDTI data.

2.1. Data acquisition

Ten healthy and five porcine hearts with chronic myocardial infarction (9 weeks after 120 min occlusion of the left circumflex coronary artery) were imaged on a clinical 1.5 T MR system (Achieva, Philips Health-Care, Best, the Netherlands) using an 8-channel head coil. The hearts were arrested with a potassium-chloride overdose, explanted and fixated by retrograde perfusion

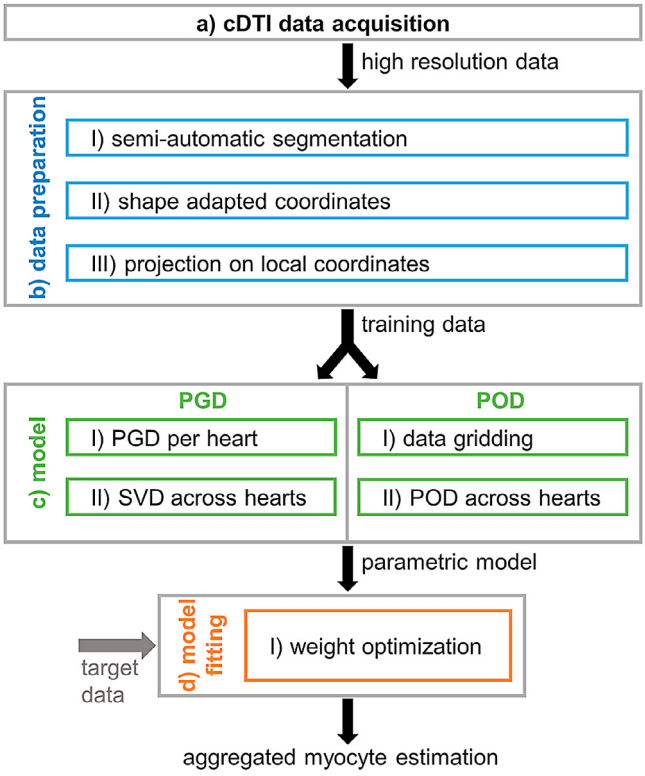

Fig. 1. Workflow: (a) High-resolution data acquisition. (b) Segmentation and definition of a shape-adapted coordinate system. (c) Extraction of a reduced-order basis of myocyte orientation by combined PGD/SVD or a POD forming a parametric model. (d) Parameter fitting of the resulting parametric models to measurement data.

(150–180 cm water column) approximately 15 min after arrest with the 4% formalin solution. During fixation, the aorta, pulmonary veins and venae cavae were clamped to ensure fixative perfusion through the microvasculature bed and to keep both ventricular chambers under hydrostatic pressure for shape preservation. Experimental procedures were in accordance with the Swiss animal protection law and conformed to Directive 2010/63 EU of the European Parliament and of the Council on the Protection of Vertebrate Animals used for experimental and other scientific purposes. Imaging was performed using a 3D multi-shot diffusion-weighted spin echo sequence with echo planar imaging readout and the following parameters: spatial resolution $0.75 \times 0.75 \times 0.75$ mm^3 zero-filled to $0.5 \times 0.5 \times 0.5$ mm^3, TR/TE 1 s/84 ms, one unweighted ($b = 0$ s/mm^2) image volume, 8 diffusion encoding directions at $b = 150$ s/mm^2 and 24 directions at $b = 1000$ s/mm^2, number of EPI profiles 25, bandwidth 664/21 Hz (freq./phase encoding), 2 signal averages. The total scan duration ranged from 20 to 24 h. Signal to noise ratio (SNR) was estimated by computing the mean signal divided by the standard deviation of noise within the masked myocardium, for the $b = 0$ image and the diffusion weighted images. To this end, the mean signal was computed on the averaged magnitude data (Firbank et al., 1999; Murphy et al., 1993). To ensure Gaussian noise distribution, the two signal averages, containing uncorrelated noise, were subtracted and the standard deviation of the difference signal was computed across the myocardium.

Data was split into three groups, eight healthy data sets were used to derive the parametric myocyte model (training), two healthy hearts were used as test cases (test). Five hearts with chronic myocardial infarction were used for testing model robustness to pathology involving remodelling (infarct). The structural

reorientation in the infarction region results in a locally, non-coherent microstructure orientation, not following the double helical pattern (Sosnovik et al., 2009; 2014; Mekkaoui et al., 2018). Thus, by fitting the model to these hearts, we can investigate the flexibility of the model and the global influence of local variations. cDTI images of one human ex-vivo data set available online on the Cardiovascular Research Grid (http://cvrgrid.org/data/ex-vivo) were used to test the potential for human heart models.

2.2. Data preparation

Data preparation includes semi-automatic segmentation of the LV myocardium, assignment of shape-adapted coordinates, and projection of the first cDTI eigenvector onto a local coordinate system.

The semi-automatic segmentation of the LV myocardium combines graph-based segmentation using manually selected seed points (Canny, 2004) and edge detection methods (Lim, 1990; Parker, 2010). Additional information from cDTI such as fractional anisotropy (FA) and first eigenvector orientation of the diffusion tensor are used to exclude trabeculae and papillary muscles. The final segmentation is manually corrected.

Secondly, a shape-adapted physiological coordinate system is derived, defining each position by a transmural, circumferential and longitudinal coordinate. This global LV coordinate system ensures that the same positions with respect to the LV anatomy are assigned the same coordinates across individual heart shapes. To this end, three linear heat transfer problems with Dirichlet boundary conditions are solved (Bayer et al., 2012; 2018; Doste et al., 2019), one for each coordinate, respectively. For the transmural (t) coordinate, the epi- and endocardial walls are used. For the circumferential (c) coordinate, two heat transfer problems are solved with Dirichlet boundary conditions prescribed at a plane through the anterior left ventricular- right ventricular (LV-RV) intersection and the apex, splitting the ventricle into half. For the longitudinal (l) coordinate, the Dirichlet boundary condition is prescribed at the LV base and a transmural cylinder at the apex. The global shape-adapted coordinates are obtained by tracking the flux directions from one boundary to the other and normalizing to the local maximal path length. This normalization compensates for the non-linearity of the solution of the heat transfer problem, similarly to normalizing the longitudinal coordinate by sampling along the shortest geodesic curve suggested by Bayer et al. (2018) and Paun et al. (2017). In addition to the global shape-adapted coordinates, the heat flux directions in longitudinal and circumferential directions and the orthonormal, transmural direction define a local coordinate system $\left(\vec{t}, \vec{c}, \vec{l}\right)$. The diffusion tensor's first eigenvector $\vec{f}$ is projected onto the axes of the local coordinate system $f_d = \vec{f} \cdot \vec{d} / \left|\vec{d}\right|$ with $\vec{d} \in \left\{\vec{c}, \vec{t}, \vec{l}\right\}$, defined at each voxel center. To account for the sign invariance of the eigenvector, the sign is chosen such that the circumferential projection is positive ($f_c > 0$).

2.3. Low-rank parametric aggregated myocyte model

The high-dimensional myocyte aggregate orientation information was compressed into a parametric, low-rank model, for each component (f_c, f_t, f_l) independently. Two reduction techniques, a combined PGD/SVD approach and POD, were compared. The approximated myocyte orientation is assembled, combining the models for each projection and the local coordinate system, $\vec{f} = \sum_{d=c,t,l} f_d \cdot \vec{d}$.

2.3.1. Combined PGD and SVD approach

A low-rank representation without any prior assumptions is extracted for each heart separately using PGD (Genet et al., 2015b). The PGD approximates the data as a sum of basis functions (modes). N_{PGD} is the number of basis functions used in the approximation. Each basis function is a product of three one-dimensional functions of each physiological coordinate. Each projection of the myocyte aggregate orientation can thus be obtained as

$$f_{d;\text{PGD}}(t,c,l) = \sum_{m=1}^{N_{PGD}} F_m(t) \cdot G_m(c) \cdot H_m(l). \tag{1}$$

Each one-dimensional function $X(d) \in \{F_m(t), G_m(c), H_m(l)\}$ is obtained as the linear combination of an individual set of N piecewise linear Galerkin basis functions $\phi_{X,k}(d)$ and scalar degrees of freedom $a_{X,k}$, such that $X_m(d) \approx \sum_k \phi_{X,k}(d) \cdot a_{X_m,k}$, for . In the transmural direction, for example $F_m(t) \approx \sum_k \phi_{F,k}(t) \cdot a_{F_m,k}$. The Galerkin basis functions $\phi_{X,k}$ in each direction depend on the number of degrees of freedom N, set to 14, 24 and 10 in transmural, cirumferential and longitudinal direction, respectively. Tests with higher number of degrees of freedom showed no significant improvements of the residual error. The degrees of freedom $a_{X,k}$ are calculated in an iterative process, minimizing the L_2-distance to the data until the relative residual variation is below 0.01. In each iteration step, $F_m(t)$, $G_m(c)$, $H_m(l)$ are optimized sequentially through a Greedy algorithm (Genet et al., 2015a; Chinesta et al., 2014a).

We exploit the structural similarity across hearts to parametrize the resulting low-order representation provided by the degrees of freedom extracted with the PGD: $a_{F_m,k}, a_{G_m,k}, a_{H_m,k}$. An SVD across hearts is applied to these degrees of freedom of the one-dimensional functions of the PGD basis, after subtracting the mean over the database. Each 1D function is represented by a set of SVD basis functions. N_{SVD} is the number of SVD basis functions representing one 1D function of the PGD basis, e.g., $F_m(t) = f_{m,mean}(t) + \sum_{n_f=1}^{N_{\text{SVD}}} w_{F_m,n_f} \cdot f_{m,n_f}(t)$. The SVD basis functions f_{m,n_f}, g_{m,n_g}, h_{m,n_h} represent the major feature variations across hearts. The resulting representation is

$$\begin{aligned} f_{d;\text{PGD}}(t,c,l) = \sum_{m=1}^{N_{\text{PGD}}} \Bigg[& \left(f_{m,mean}(t) + \sum_{n_f=1}^{N_{\text{SVD}}} w_{F_m,n_f} \cdot f_{m,n_f}(t) \right) \\ & \cdot \left(g_{m,mean}(c) + \sum_{n_g=1}^{N_{\text{SVD}}} w_{G_m,n_g} \cdot g_{m,n_g}(c) \right) \\ & \cdot \left(h_{m,mean}(l) + \sum_{n_h=1}^{N_{\text{SVD}}} w_{H_m,n_h} \cdot h_{m,n_h}(l) \right) \Bigg]. \end{aligned} \tag{2}$$

A minimization problem can then be solved to identify the weights w giving the best fit to the data.

2.3.2. POD approach

To extract a low-order representation using a POD (Buljak and Maier, 2011; Buoso et al., 2019), each data set is interpolated onto a common grid $\left[t_i, c_j, l_k\right]$ exploiting the shape-based coordinates described in Section 2.2. We selected $i = 1, \ldots, 20;\ j = 1, \ldots, 200;\ k = 1, \ldots, 120$. Snapshots of the data, obtained from 20 iso-surfaces with constant transmural coordinate for all training hearts, are used to build a snapshot matrix $S = [s_i],\ i = 1, \ldots, n_s$, with n_s = number of slices with transmural normal×data sets = 20×8. Each snapshot, s_i, is composed of $n_d = \max(j) \times \max(k) = 24,000$ discrete points. The POD bases $\Phi = [\Phi_1, \ldots, \Phi n_s]$ are computed from an eigenvector decomposition of the correlation matrix $C = S^T S$ and sorted by decreasing singular value,

$$\Phi_i = \frac{1}{\sqrt{\sigma_i}} \cdot \mathbf{S} \cdot \vec{\xi}_i,\ i = 1, \ldots, n_s, \tag{3}$$

with singular values σ_i and eigenvectors ξ_i. For the reduced-order myocyte model, the POD basis is truncated. N_{POD} is the number of included basis functions. The resulting model for each aggregated myocyte projection is

$$f_{d;\mathrm{POD}}(t_i, c_j, l_k) = \sum_{m=1}^{N_{\mathrm{POD}}} \left[\left(w_{m,t_i} \cdot \Phi_m(c_j, l_k) \right) \right]. \quad (4)$$

2.4. Model fitting

For personalization of the aggregated myocyte model (PGD: Eq. (2) or POD: Eq. (4)), the weights (PGD: w_{F_m,n_f}, w_{G_m,n_g}, w_{H_m,n_h} or POD: w_{m,t_i}) are fit to measured data.

Computational cost can be split into the time needed for model extraction from the training data and the time for weight adaptation and reconstruction of the estimated myocyte aggregate orientation field. Times were measured on an 8-core Intel(R) Core(TM) i7-10700 K, 3.8 GHz desktop computer. The PGD of a volumetric data set took 65 min for each projection, on average, without parallelization. Reconstruction of the PGD model took 16.3 min for 900,000 data points, on average. For the PGD model, a PGD of the target data has to be performed prior to model fitting. Computation of the POD took 2 min for each projection, on a single core. POD model reconstruction took 20 s and did not require a preceding POD of the target data.

2.4.1. Combined PGD and SVD approach

A PGD is applied to the available data. Weight adaptation of the SVD basis functions used in the parametric model is done by minimizing the error to the low-rank PGD representation of the data in a least squares sense. The number of SVD basis functions is chosen to be the same for all one-dimensional functions within PGD basis. The same number of SVD and PGD basis functions are used for all three projections of the myocyte aggregate orientation. The resulting number of parameters in the model is $N_{\mathrm{SVD}} \cdot N_{\mathrm{PGD}} \cdot 3(\text{1D-functions}) \cdot 3(\text{projections})$.

2.4.2. POD approach

The model parameters are calculated by projecting the measured data onto the reduced POD basis used in the model Eq. (4). The number of weights to fit is $N_{\mathrm{POD}} \cdot 20(\text{transmural slices}) \cdot 3(\text{projections})$.

2.5. Error metric

To evaluate the model estimations of the principle myocyte aggregate orientation (MA), we compare the angular difference between the approximation at the positions of the voxel centers to the first eigenvector of the diffusion tensor from the high-resolution measurements (ΔMA). As an error metric, the median over all data points on the myocardium is used. For qualitative evaluation and visualization we show helix angle maps. The helix angle is defined as the angle between the local circumferential axis and the projection of the principle myocyte direction onto the local longitudinal-circumferential plane (Stoeck et al., 2018; Scollan et al., 1998).

2.6. Comparison to other models

We compare our data-driven low-rank basis model to two state-of-the-art approaches to generate a vector field of aggregated cardiomyocyte orientation, a rule-based model based on Bayer et al. (2012) (RBM) and an atlas extracted from the healthy training data set.

2.6.1. Rule-based model (RBM)

The rule-based model is based on Bayer et al. (2012) and is adapted to the LV only. To obtain the local aggregated myocyte orientation the local coordinate system (section II.B) was rotated. The circumferential axis was counterclockwise rotated by the local helix angle around the transmural axis, and subsequently by the local transverse angle around the longitudinal axis. The local helix and transverse angle are linear functions of the transmural coordinate. To personalize the rule-based model to the porcine data, the boundary conditions of helix and transverse angle at endo- and epicardium were adapted to the cDTI data sets, applying a least-square fit of the linear functions.

2.6.2. Atlas of aggregated myocyte orientation

We use the shape adapted global coordinates to map the aggregated myocyte orientation across the training population onto a common grid. This step replaces the registration to an common average geometry, used in most state-of-the-art atlas methods. This ensures that no bias is introduced due to change of the method used for mapping. The same common grid as for the POD method is used (section 2.3.2). The local average aggregated myocyte orientation is computed at each grid point.

3. Results

SNR of the DTI data was 38.7 ± 9.5 at $b = 0$ s/mm^2, 34.6 ± 8.3 at $b = 150$ s/mm^2, and 19.9 ± 4.3 at $b = 1000$ s/mm^2.

The three 1D functions composing the first PGD mode generated with one SVD mode are visualized in Fig. 2(a). Comparing the assembled 2D PGD mode without transmural component to the first POD mode in Fig. 2(b) shows a similar pattern for POD and PGD. However, for the transmural and longitudinal projections, the corresponding POD modes show more local variations and are less smooth.

Fig. 3 (a) shows the median ΔMA as function of the number of modes. ΔMA reduces within a few modes and reaches a plateau. With 4 PGD and 4 SVD modes the median ΔMA is 11.5°. The number of included PGD modes has a higher influence as compared to the number of SVD modes. Additional modes result in improvements of less than 3.5% per added PGD mode and less than 2.6% per added SVD mode. The brown isoline of 0 SVD modes in the surface plot shows the results using the mean PGD modes without personalizing the model with the SVD modes. This can be considered as a low-rank atlas obtained from PGD. Personalizing the model with only one SVD mode improves the error by 6.5%(1.3°) for the first PGD mode and more than 14% when more than one PGD mode is included. Comparing ΔMA at the beginning of the plateau (4 PGD and 4 SVD modes) to the PGD model with the same number of PGD modes without personalization (4 PGD and 0 SVD modes), personalizing the model improves the error by 35.6%(6.3°). For the POD model, the median ΔMA decreases to 11.3° for 8 POD modes, employing more modes improve the error by less than 2.5% per mode.

Considering the healthy test data, with the PGD model, the median ΔMA is within the range of the error for the training cases. When using more than 3 PGD modes and 4 SVD modes the error changes by less than 0.2° per mode. Using the POD-based model, including more than 8 modes decreases the error by less than 1% per mode. For 8 POD modes the average over the healthy test set shows an offset of 2.2° compared to the training data set.

When the model is fit to the data set with chronic myocardial infarction we observe similar accuracy as for the healthy test set for both models (increase in ΔMA$<1.5°$ compared to the healthy test set).

In Fig. 3(b) histograms of ΔMA are presented for the training data, showing the change of the error distribution with increasing

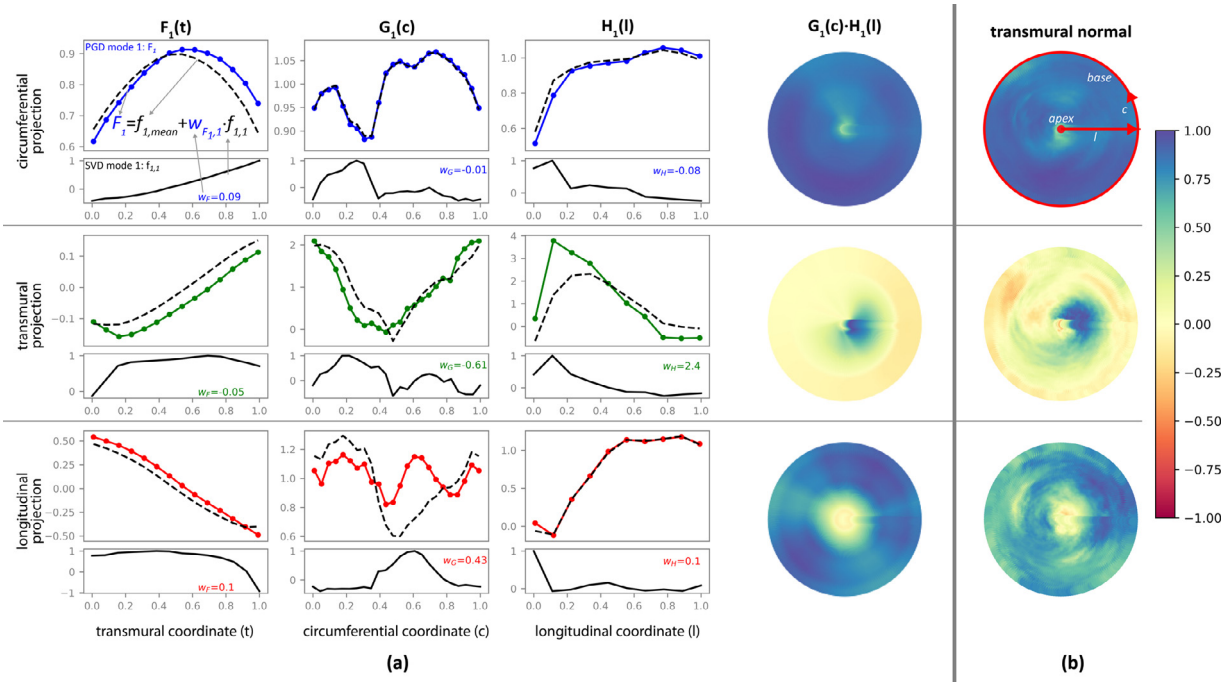

Fig. 2. Example of (a) first PGD mode and first SVD mode; (b) first POD mode. The rows correspond to the decomposition of the principle myocyte direction (circumferential: f_c, transmural: f_t, longitudinal: f_l). Each PGD mode is a product of three 1D functions (F(t), G(c), H(l)) (coloured curves). Each 1D function is a sum of the population mean (dashed line) and the SVD mode (black line) weighted with a case adapted parameter. For illustration, the 2D PGD mode without transmural component is assembled and compared to the unweighted 2D POD mode shown in the two most right columns. Both modes are normalized to their maximal absolute values.

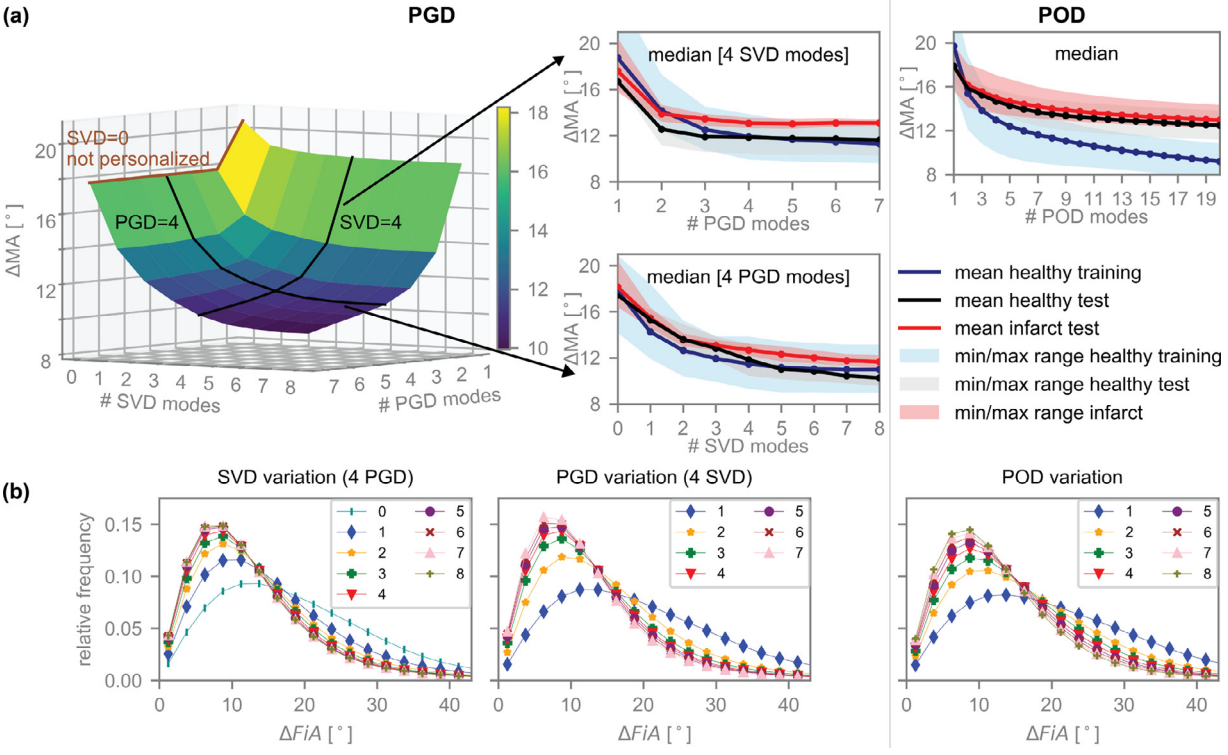

Fig. 3. (a) Median ΔMA across the myocardium as function of number of modes for the combined PGD/SVD and the POD model. The surface plot on the left shows the median ΔMA averaged across the training cases. The black iso-lines indicate the positions of the example line plots in the second column with fixed number of 4 SVD and PGD modes, respectively. The line plots represent the median ΔMA averaged over the training cases in blue, the healthy test set in black and the infarct test cases in red. The shaded area depict the minimum to maximum range. The variation of ΔMA with the number of POD modes is show on the right. (b) Normalized histograms of ΔMA as function of number of modes (colour coded). Data is bin-wise and averaged across the training data. (For interpretation of the references to colour in this figure legend, the reader is referred to the web version of this article.)

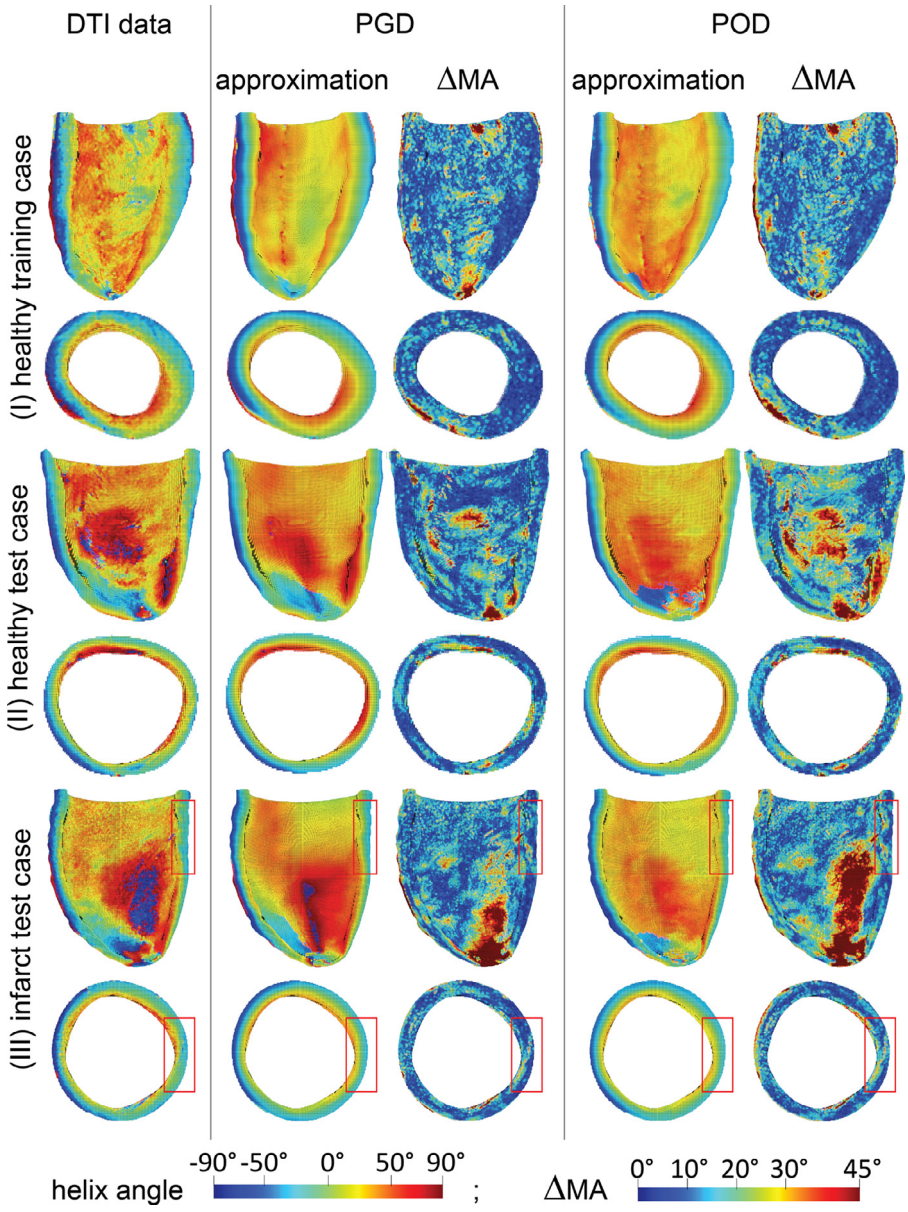

Fig. 4. Helix angle distribution across the myocardium for one heart from the training data set, one from the test set and one heart with chronic myocardial infarction. A long-axis cut through the septal (left) and free wall (right) as well as one mid-ventricular short-axis cut are presented. The helix angle maps of high-resolution cDTI measurements (left column), PGD (mid) and POD (right) model approximations are shown, together with ΔMA for the PGD and POD method. The red boxes indicate the region of the infarction.

number of modes. Adding the second mode shows the most significant improvement for both PGD and POD. For all data sets, when adding a second mode the median error decreases by more than 22%/9.5% and the interquartile range (IQR) reduces by more than 24%/17% for PGD/POD respectively. Convergence of the error distribution is observed with 3–4 modes (PGD, SVD and POD), adding more modes leads to improvement of IQR and median less than 0.6° per mode.

The following evaluation is done using the optimal mode configuration, resulting in the smallest median ΔMA averaged over the training data, of 7 PGD and 7 SVD modes. The median ΔMA is below 12° for all investigated cases, with an average of 10.3° over all cases. For the POD method 8 modes are used to prevent overfitting to the training data, resulting in a maximal median ΔMA of 15.7°, with an average of 12.5° over all cases. For the choice of 8 POD modes, the number of weights are similar for both methods (POD: 480; PGD: 441).

To validate if the randomly selected healthy test data set is a representative choice, we performed a cross-validation and calculated the mean over all permutations of splitting the ten healthy hearts into a test set with 2 cases and a training set with 8 cases. At the optimal mode configuration of 7 PGD and 7 SVD modes or 8 POD modes the median ΔMA averaged over the healthy test set used in the analysis presented in this paper is PGD:10.1°/POD:13.5°. This is 1.7°/0.3° lower than the average over all permutations (mean ± std: PGD: $11.8 \pm 1.2°$; POD: $13.8 \pm 1.4°$). This reflects a small positive bias of the randomly selected healthy test for the PGD model.

Fig. 4 shows the helix angle mapped onto the myocardium comparing the measurements and the model estimation for one heart from the training data set, the healthy test set and the infarct data set, respectively. Largest differences can be observed at the apex for all cases. Both models smooth the data, but retain dominant tissue characteristics. The original data shows 180° flips

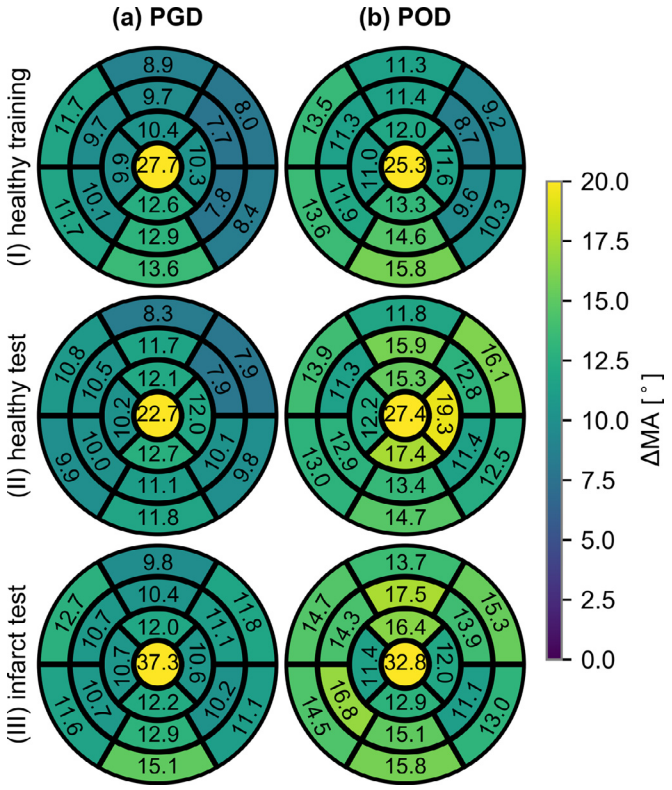

Fig. 5. Median of the angular difference between the model estimation and the cDTI measurements in the AHA zones, sector-wise averaged over the healthy training data set (I), healthy test case (II) and infarct test set (III). The columns represent ΔMA using (a) the PGD/SVD-based and (b) POD-based model.

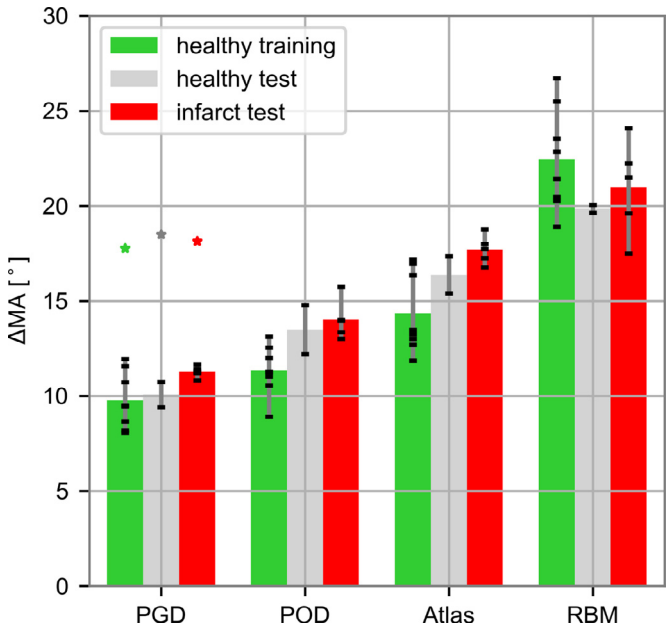

Fig. 6. Comparison of data-driven PGD and POD model to atlas and RBM. The bars represent the median over the myocardium of ΔMA. In green, averaged over the training data, in grey for the healthy test set and in red for the infarct test set. The whiskers show the maximal spread over the cases, the black markers indicate the individual cases. The green, grey and red stars indicate the averaged ΔMA for the un-personalized, low-rank PGD model. (For interpretation of the references to colour in this figure legend, the reader is referred to the web version of this article.)

at the endocardial wall, due to the not cyclic definition of the helix angle ($+90°\|-90°$). These are smoothed out in the reconstruction for both models, visible as pronounced errors $>45°$ in the ΔMA maps. Both models tend to underestimate the steepness of the helix at the endo- and epicardial walls. The region of the myocardial infarction does not show a prominent error.

For quantitative evaluation, a sector-wise analysis of ΔMA is shown in Fig. 5. Each sector represents the median error across each AHA zone (Cerqueira et al., 2002) averaged over the cases. The error in the apical segment (number 17) is more than 1.4 times higher than in all other segments, for all cases. To evaluate the variation between the hearts we computed the sector-wise standard deviation (std) across data sets, excluding the apex. The inter-case variation is lower for the PGD than for the POD model for all data sets (PGD/POD $\text{mean}_{\text{sector}} \pm \text{std}_{\text{sector}}$: training: MA: $2.1 \pm 0.7°/2.6 \pm 0.8°$; healthy test: MA: $1.1 \pm 0.8°/2.1 \pm 2.6°$; infarct test: MA: $1.4 \pm 0.6°/2.7 \pm 1.4°$). The sector-wise averaged error shows a similar distribution over the AHA zones for training and test sets, using the PGD model. The difference angles are smaller at the free wall, than at the septal wall. The standard deviation over the AHA segments (excluding the apex) averaged over the cases, quantifies the homogeneity across the myocardium: PGD/POD: $\text{mean}_{\text{case}} \pm \text{std}_{\text{case}}$: training: MA: $2.3° \pm 0.7°/3.0° \pm 0.6°$; healthy test: MA: $1.8° \pm 0.0°/3.9° \pm 0.5°$; infarct: MA: $1.9° \pm 0.2°/3.4° \pm 0.7°$. The mean std across sectors is below 4.2° for both methods and all data sets. For the infarct test set, the error in the manually segmented infarction region is higher when compared to the healthy remote region for 3 out of 5 cases with an average across cases of: PGD/POD $\text{mean}_{\text{case}} \pm \text{std}_{\text{case}}$: MA: $1.2° \pm 1.9°/2.0° \pm 4.2°$. A high variation of the error difference between infarct and remote zone is present. Ranging from a smaller error in the infarction with: PGD/POD ΔMA: 1.1°/3.8° to a higher error in the infarction with a maximum difference of: PGD/POD ΔMA: 3.8°/8.3°. For three cases the difference is within the standard deviation over the AHA sectors for the healthy test cases, measuring the spatial variation of the error.

To compare personalization of the data-driven PGD and POD models with an atlas-based method, as well as compare the spatial flexibility of the PGD and POD models with the rule-based method, global estimation errors were compared. The comparison of ΔMA between the approximations of the PGD model, POD model, atlas, and rule-based methods is presented in Fig. 6. The PGD model shows the smallest average error for all data sets, healthy training data, healthy test set and infarct test set, respectively. ΔMA is 9.7°, 10.1° and 11.3° when averaged over the training cases, healthy test case and infarct test cases, respectively. The error is higher for the POD model, followed by the atlas and RBM. Compared to the error using the PGD model, the average error is 34% higher for the POD model, 62% higher for the atlas and 97% higher for the RBM for the healthy test set. For PGD model, POD model and atlas the error for the training data is smaller than for the test sets with a difference of less than 2.1°, whereas for the RBM, not derived from the training data, the average error on the training data set is 2.6° higher. ΔMA averaged over the infarct test set is higher than the average over the healthy test cases for all methods by less than 1.5°. The un-personalized PGD model, shown as markers in Fig. 6, performs worse than the personalized PGD and POD models, indicating the need for personalization. For the healthy test set the gain in ΔMA by personalization is 45% for the PGD model and 27% compared to the POD model. Due to smoothing by dimensionality reduction, ΔMA for the un-personalized PGD model is higher than for the atlas. For the healthy test set, ΔMA is 11% smaller for the atlas, compared to the un-personalized PGD model. The personalized rule-based approach shows a higher ΔMA by 7%, compared to the un-personalized PDG model, for the healthy test set.

To analyze the spatial error distribution for the PGD, POD, Altas, and RBM approximations, Fig. 7 shows box plots of ΔMA for

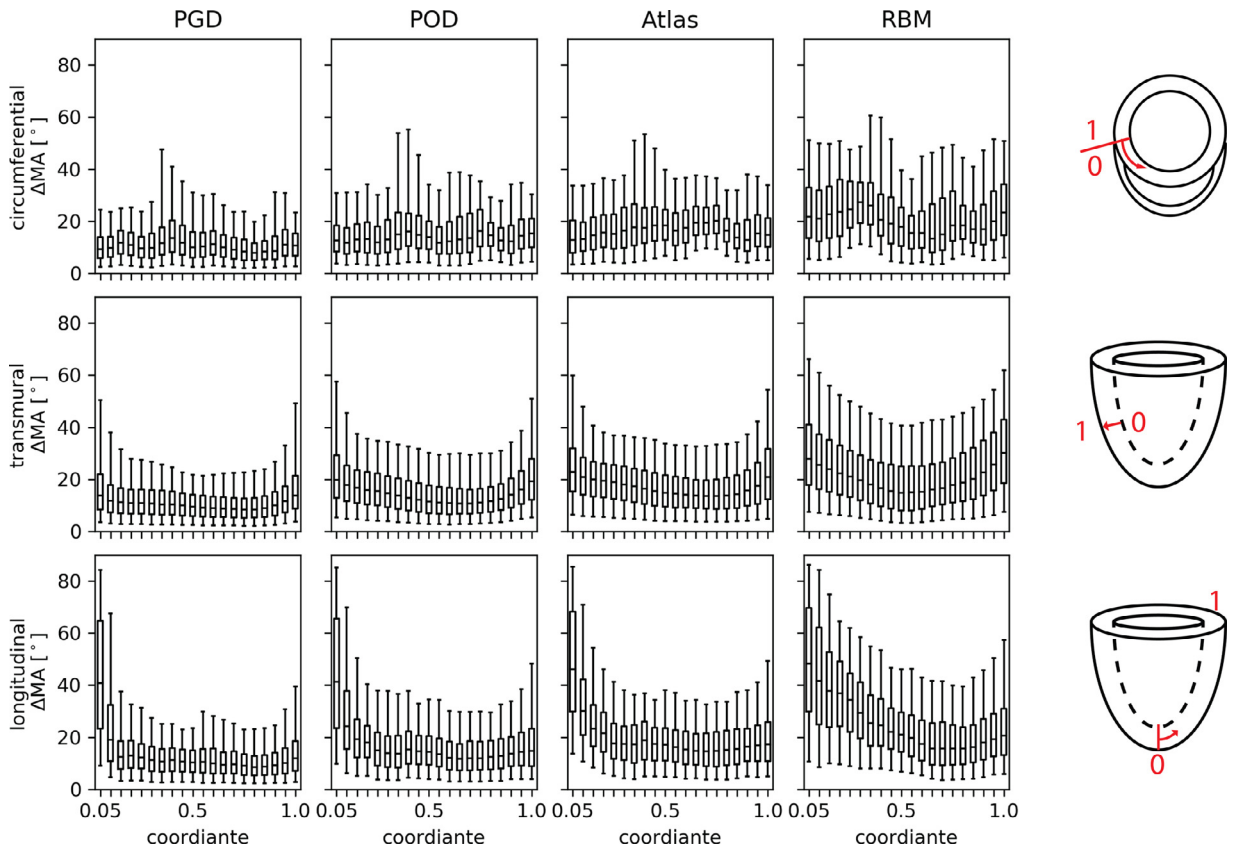

Fig. 7. Spatial variation of the angular difference between the model estimation and the cDTI measurements. The columns show the results using the PGD model, POD model, atlas, and RBM. The rows present the error variation along the circumferential, transmural, and longitudinal coordinate. For each direction, the data was assigned to 20 bins, each represented by one box plot. Each box plot shows the median, 25-, 75- (box), 5-, and 95- (whisker) percentiles obtained for each case and averaged over the healthy test data set.

20 bins along the circumferential, transmural, and longitudinal coordinate. The plots evaluate the error for the healthy test cases. The analysis for the training and infarct test cases show similar trends and are presented as supplementary material. The circumferential variation shows an elevated error for bins between circumferential coordinate $c = 0.3$ and $c = 0.4$ with a significant peak of the 95-percentile. This circumferential coordinate is correlated with the position of the inferior LV-RV intersection. A less significantly elevated error with increased 25- and 75-percentile values is present at $c = 0.55 - 0.6$ for approximations using the POD, atlas, and RBM. A local error maximum is present for all models around the anterior LV-RV intersection ($c < 0.1/c > 0.9$). The transmural error variation shows a u-shaped trend with the highest error at the endocardium ($t = 0$), and similarly high error at the epicardium ($t = 1$). The change towards the smallest error at mid myocardium differs between the models. For the PGD, POD and atlas a rapid decrease of the 95-percentile within the outermost 15% at both endo- and epicardium is observed. For the PGD model, all percentiles decrease within this outer area. Whereas, for the POD and atlas approximations the median, 25- and 75- percentile decrease with lower gradient toward mid-myocardium. The minimum error is present closer to the epicardium ($t = 0.6$). For the RBM all percentiles decrease more slowly, nearly linearly to the minimum at mid myocardium ($t = 0.5$). The longitudinal variation presents a distinct peak at the apex ($l < 0.05$) for all models. For the PGD model the error decreases with a steep gradient and levels of at $l = 0.15$. For POD and atlas approximations the error halves within the two most apical bins ($l < 0.1$). However, an elevated error is visible in the apical third of the ventricle. RBM approximation shows a slow error decrease that reaches a plateau at $l = 0.65$. A small increase of the error at the base ($l > 0.85$) is present for all models. The local maxima of the transmural variation at the endo- and epicardial surfaces and the prominent peak of the longitudinal variation at the apex confirm the results shown in Figs. 4 and 5. The PGD and POD model based on basis functions extracted from porcine data have been applied to one human ex-vivo data set to test the feasibility to approximate human myocardial structure. Fig. 8 shows the same plots as Figs. 3(a), 4,5,6 and 7 for the human heart. Fig. 8(a) shows the error dependence on the number of included basis functions. The markers in the surface plot indicate the approximation of the human data without personalization of the PGD model, directly using the mean PGD modes, extracted from the porcine training data sets. The mean of the first PGD mode results in ΔMA of 16.4°. Adding more modes without personalization results in a high error of 22.7°. To compensate this deviation of mean PGD modes extracted from the porcine data and the human data, a scaling factor, estimated during fitting to the human data, was introduced for the mean. The weighted mean (0 SVD modes) results in a ΔMA of 15.19°, adding the weighted mean of higher PGD modes does not change the approximation error (improvement compared to one weighted PGD mode <0.2°). The 2-norm of the weights, scaling the 1D functions ($w_{F_m,0}, w_{G_m,0}, w_{H_m,0}$) is >0.8, for each PGD mode and each projection. Personalizing the PGD model, including weighted SVD modes, significantly reduces the approximation error to an optimum of 9.4° with 7 PGD and 8 SVD modes. A plateau of the error is reached, when 2 PGD and 4 SVD modes are used (ΔMA = 10.9°). Including more than two PGD basis functions in the model does not improve the approximation significantly (improvement< 0.5°). With a fixed number of 2 PGD modes, the first SVD mode reduces ΔMA to by 20% to

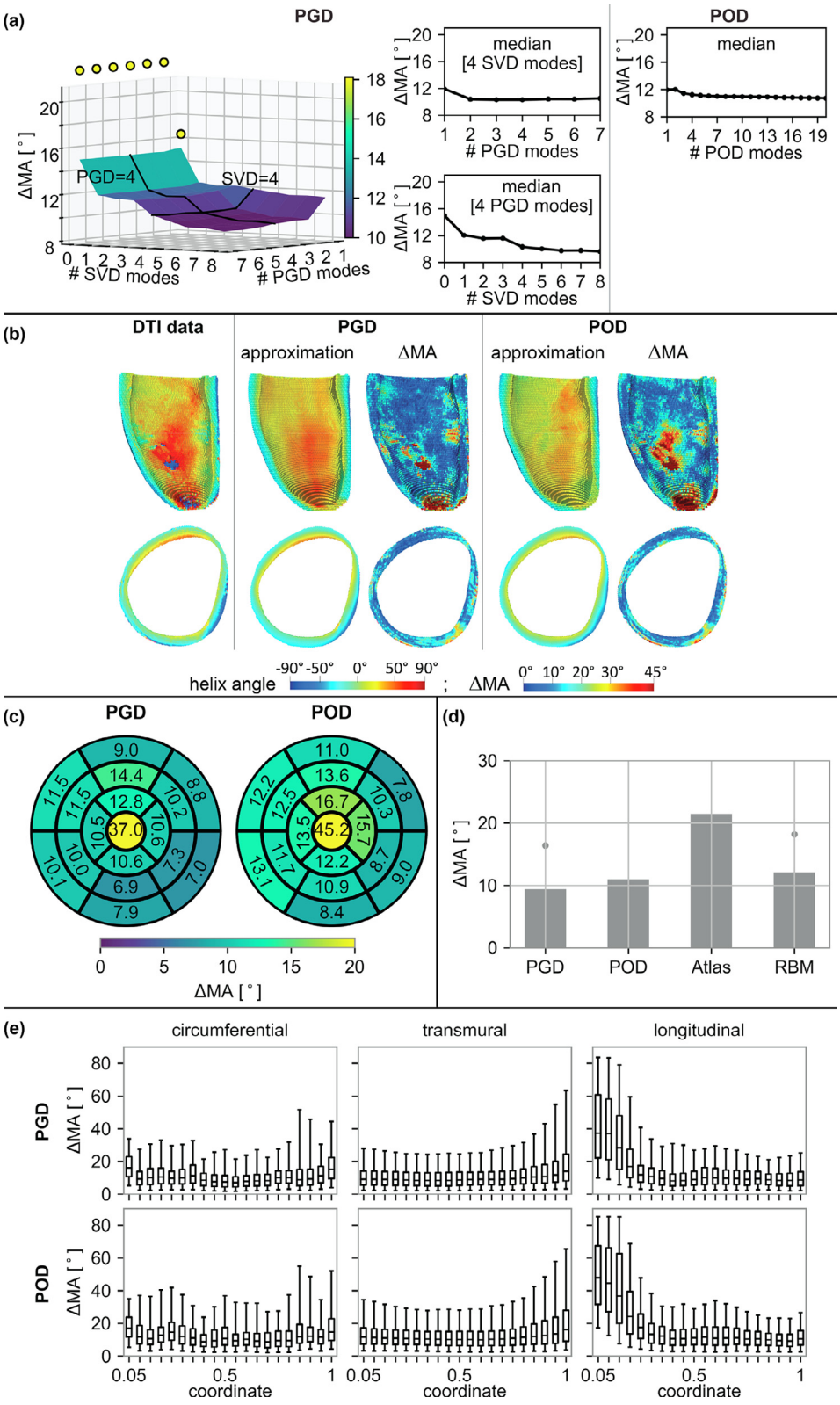

Fig. 8. Summary of PGD and POD model results applied to one ex-vivo human heart. (a) Median ΔMA across the myocardium as function of number of modes for the combined PGD/SVD and the POD model. Equivalent to Fig. 3 for the porcine data. The mean (0 SVD modes) is multiplied by a weight to adapt it to the human data. The markers in the surface plot indicate the un-personalized PGD model without weighted mean. (b) helix angle distribution across the myocardium together with ΔMA maps, as in Fig. 4 for the porcine data. A long-axis cut through the free (left) and septal (right), and one mid-ventricular short-axis cut are presented. (c) Median of the ΔMA between the model estimation and the cDTI measurements in the AHA zones. Refer to Fig. 5 for comparison to results on the porcine data. (d) Comparison of the PGD and POD model to an altas and RBM. The bars represent the median of ΔMA in the myocardium for the models personalized to the human data with the optimal mode configuration. For the PGD model, the marker indicates the un-personalized PGD model with one mode. For the RBM, the marker indicates the RBM adapted to the mean helix and transverse angles form the porcine training data set. (e) Spatial variation of the angular difference between the PGD or POD model estimation and the cDTI measurements. As for the porcine cases in Fig. 7, the data assigned to 20 bins along each coordinate axis. A box plot is show for each bin.

12.0° Adding the second and third SVD mode don't change ΔMA significantly (i.e. <0.4°). The fourth SVD mode improves the ΔMA to 10.4° and more SVD modes lead to minor improvement of less than 0.5° per mode. The POD model results in a low error of 12° with only one mode. With 11.2° for 4 POD modes the error levels off, with minor improvements of less than 0.1° per mode for higher POD modes. The helix maps in Fig. 8(b) show a qualitatively good agreement between the original cDTI data and both PGD and POD approximations. However, both models smooth the data. The cDTI data shows a small dark blue patch at the endocardial surface with negative helix angle due to its non-cyclic definition. This is not captured by both models, the POD over-smooths the helix values at the endocardium. The ΔMA maps show elevated errors at the apex and in the region with a steep helix at the endocardium, more prominent for the POD model. Qualitative results agree with observations form the porcine data sets. A quantitative, sector-wise error analysis for the AHA sectors is presented in Fig. 8(c). The apical cap shows the highest error, more than 2.5 times higher than in all other sectors. The error in the sepal wall is higher than in the free wall. To evaluate the homogeneity across the myocardium, the standard deviation over the AHA segments (excluding the apex) is computed: PGD: std(ΔMA) = 2.0°/ POD: std(ΔMA) = 2.5°. The POD model approximation is more heterogeneous across the sectors than the result of the PGD model. This standard deviation over the AHA segments is in the same range as for the healthy porcine test cases (Δ± 0.2°) for the PGD model and smaller than for the healthy porcine test cases for the POD model. A comparison of the global error, for the PGD model, POD model, atlas and RBM, for the human test case, is shown in Fig. 8(d). The bars represent ΔMA for the optimal mode configuration. The PGD model shows the best performance with ΔMA = 9.4°. The error is 17% higher for the POD model, 29% higher for the RBM model and 129% higher for the porcine atlas. The marker for the PGD model indicates the un-personalized first mean PGD mode, extracted from the porcine data. Without personalization, ΔMA is 75% higher, compared to the personalized PGD model. Personalization improves the ΔMA by 50% for the RBM, comparing the fit to the human data and the adaptation to the average boundary values from the porcine data. The RBM shows the largest improvement, when approximating the human data set, compared to the ability to represent the porcine data set. The spatial variation of ΔMA is shown in Fig. 8(e). Both models result in similar spatial variations. In contrast to the circumferential variation for the porcine data in Fig. 7, no locally elevated error is observed at the inferior LV-RV intersection. The 95-percentile value is elevated for $c > 0.8$. The transmural plot presents an error increase for $t > 0.7$ towards the epicardium, with a predominant increase of 75- and 95- percentile. The error at the endocardium is not increased for the PGD model. For the POD model the 75- and 95 percentiles show a minor increase towards the endocardium, less pronounced than for the porcine data. The longitudinal error variation shows a peak at the apex with IQR > 35°, for $l < 0.1$. For both models the error deceases with increasing longitudinal coordinate, leveling off at $l < 0.35$. The region of high errors at the apex is larger than for the porcine test cases.

4. Discussion

The small median angular difference between the measurements and the model estimations for the healthy training data set (PGD: $9.7 \pm 1.5°$ / POD: $11.3 \pm 1.3°$) as well as the rapid decline of the angular error towards a plateau with 4 PGD and 4 SVD modes show that the predominant myocyte orientation can be represented in a low-rank basis. Contrary to the PGD approach, the POD method does not present such a distinct plateau for the error as a function of number of modes, however the small improvement of less than 2.5% per added mode for more than 8 modes and the overall small median error supports the feasibility of the approach. For the combined PGD and SVD method, the PGD modes represent the major characteristics of the microstructure within each heart. Higher order modes capture the characteristics extracted from the residual and therefore reflect features with smaller global impact. The SVD modes allow for a parametrization of the PGD modes accounting for variability across hearts. Thus, the convergence with 4 SVD modes relates to the high degree of similarity of the major structural characteristics within the species. Varying the weights of the SVD modes independently in the three spacial dimensions, allows for the description of unseen combinations and structures with differently pronounced characteristics along the spatial coordinates making the approach more flexible. For the POD model, two-dimensional modes representing onion-like shells of the myocardium at different transmural depths are derived. They represent the major structural characteristics directly extracted across hearts.

The PGD model consists of the mean of the low-rank PGD basis across the training data and the SVD basis functions, responsible for adaptation of the model to new data. The first PGD mode representing the main characteristics of the structure shows the smallest gain by SVD personalization. This suggests that the most dominant structural characteristic varies less between individuals compared to more detailed characteristics. However, personalizing the model has a significant effect when using more PGD modes. In the range where the error reaches a plateau (4 PGD modes), ΔMA improves by 35.6% (6.3°) due to personalization (4 SVD modes) comparing to the results without personalization (0 SVD mode). Consequently, despite the similarity of cardiac microstructure across individuals, personalizing the common characteristics using the basis of main variations improves the representation. Personalization is of increasing importance for more detailed characteristics, thus higher PGD modes.

To evaluate the generalization of the models to unseen data, we used two healthy test cases. With the PGD model, the error for both test cases, is within the range of the error on the training data, highlighting the model's capability to represent healthy microstructure. The convergence of the error distribution for 3 PGD modes (with 4 SVD modes), and an improvement with a higher number of SVD modes (for 4 PGD modes) suggests that more than 4 SVD modes are needed to capture the variation of more detailed structural characteristics. However, for 5 and more SVD modes (with 4 PGD modes), the relative frequency of angles smaller than 12.5° is higher than on the training data, confirming a good fit of the model to unseen data. The POD model shows no significant (< 2.5%/added mode) improvement of the angular error when using more than the first 8 out of 160 modes for the test cases. To prevent over-fitting to the training data this number of modes can be chosen as an upper limit for the number of included basis functions. The error increment of 2.2° for the median ΔMA between training and test data suggests a lower fit quality to new data compared to the combined PGD and SVD approach. However, the median error (ΔMA = 13.5° for 8 POD modes) stays in a feasible range.

The fit of both models to hearts with chronic myocardial infarction shows a minor additional error < 1.5% across the myocardium compared to the healthy test cases. This indicates that both models are capable of parameterizing the global structural variability of the diseased hearts investigated, with local chronic myocardial infarction. For the PGD model the median error for all infarct cases is within the range of the healthy training cases, with small variation between cases. The scar region covers $7.1 \pm 2.8\%$ of the myocardium and has a mass of 5.4 ± 2.4 g. The local error in the area of the infarction is slightly higher compare to the remote healthy myocardium (case average: PGD: 1.2°/POD: 2.5°). This variation is

within the range of the standard deviation over the AHA sectors for the healthy test cases, approximating the local in-homogeneity across the myocardium. However, for two out of five cases the local error in the area of the myocardial infarction is higher, with maximal difference values of ΔMA PGD: 3.8°/POD: 8.3°. This locally elevated error within the infarction may be attributed to (a) a pathologically reduced fractional anisotropy and thus larger variability in eigen vector orientations derived from noisy cDTI data and (b) structural characteristics in the area of the myocardial infarction, not represented by the models derived from healthy training cases. All methods investigated show a similar median error offset compared to the healthy test set. This suggests a small global effect of the chronic myocardial infarction.

Comparing the data-driven models obtained using two different order reduction methods, the combined PGD and SVD model shows a smaller estimation error in all sectors of the myocardium, compared to the POD model, for all data sets. The difference between methods is more pronounced for the test cases. Additionally, the error variation across sectors is lower for the PGD and SVD method compared to POD. This emphasises the higher flexibility of the PGD method to capture variations. The a priori method (PGD) extracts a low-rank approximation of data without prior assumptions about the tissue structure. Using an SVD, each one-dimensional function is parametrized independently. The 2D POD is directly applied across all sliced training data sets, resulting in modes with a fixed 2D pattern. The modes are *a posteriori* weighted to approximate new data. 2D patterns that have not been seen before are fit less precisely. The POD has the advantage of being faster when approximating new data. For the combined PGD and SVD method, prior to the weight adaptation, a PGD of the new data is required.

The randomly selected healthy test set used in this analysis includes a small positive bias of 1.7° for the PGD model, compared to the averaged cross-validation across the healthy cases. The minor positive bias for the POD model of 0.3° is within the standard deviation over the permutations and can thus be neglected. All comparisons to other methods were performed with the same healthy training and test set. However, assuming a higher independence to the choice of the data sets for atlas and RBM, the additional error for the PGD model on the test set would correspond to an error increase of 16.8%, this is significantly smaller than the additional error for the other methods evaluated: POD:34%; atlas:62%; RBM: 97%. To this end, the positive bias does not distort the evaluation results.

The PGD and POD model approximate the underlying data sets better than the two investigated state-of-the art models, namely an average atlas extracted from the same training data and a rule-based approach (RBM). The PGD model performed the best, indicating a high flexibility to better capture more local variations due to its three independently varied one-dimensional functions of spatial coordinates. The POD and atlas model show a very similar spatial error variation, with the POD model resulting in smaller errors. The advantage of the altas method lies in providing 3D information with good spatial coverage, resulting in a spatially detailed average structural representation, however without the possibility for personalization. The POD modes constructed are 2D, trading the correlation of information along the third spatial direction for the option to personalizing the POD model. Consequently, the POD model using only one mode would perform worse than a 3D atlas. In order to provide three dimensional modes a 3D POD could be performed requiring a larger amount of available training data. The results indicate that benefit of personalization is higher than the information loss due to truncation of the POD basis. The linear RMB simplifies the aggregated myocyte orientation field losing local spatial information. This results in the highest median error of the methods compared, for all underlying cases and less localized elevated errors with larger regions of increased error towards the endo- and epicardium and in the lower halve of the ventricle towards the apex.

All investigated methods have limitations at the apex, the endo- and epicadial surface and the inferior LV-RV intersection. The highest errors are present at the apex ($l < 0.05$), comparable to previously reported high inter case variability at the apex by Lombaert et al. (2012). Potential confounders include (a) a higher degree of uncertainty in the input data due to partial voluming effects (b) a more error prone segmentation in the apical region (c) potential structural differences in the apical region between hearts affecting the possibility of extracting a general basis (d) a reduced density of data points in the transmural-longitudinal plane towards the apex, resulting from the LV geometry. The latter is not taken into account for the choice of the support of the Galerkin basis for the PGD approach nor for the grid used with the POD and atlas method. The endo- and epicardial surfaces are equally prone to partial voluming effects and segmentation errors, especially at the intersection with papillary muscles at the endocardium. These regions of more longitudinal aggregated myocyte orientation are not localized at the same positions across hearts and are very local often without smooth spatial transition. Both PGD and POD models over-smooth these regions. The 2D modes of the POD model are less flexible to capture the variation of 2D patterns in detail. The local error peak along the circumferential coordinate at $c \sim 0.4$ correlates with the position of the inferior LV-RV intersection and might be attributed to the varying length of the septum, influencing the representation of microstructure at the LV-RV intersection. Even so, our methods show good results on both the healthy and infarct test set, to improve the robustness of the method and be able to draw statistical conclusions, an increased cohort would be desirable.

Previous studies (Nikou et al., 2016a; Pluijmert et al., 2017; Palit et al., 2015a; Rodríguez-Cantano et al., 2019; Eriksson et al., 2013) agree on the sensitivity of cardiac biomechanics on microstructure orientation. However, the required accuracy of myocyte aggregate orientation that is sufficient for robust simulations, highly depends on the parameter of interest and the underlying model. In electrophysiolgy, Vadakkumpadan et al. (2012) found that a mean helix angle difference of 15.4° has no significant influence on activation maps and pseudo-ECG in ventricular tachycardia and sinus rhythm, at a clinical observable level. Studies on cardiac mechanics revealed a sensitivity of active stress, strain and stress distribution to errors of approximately 10° (Palit et al., 2015b; Pluijmert et al., 2017; Geerts et al., 2003). A sensitivity study by Rodríguez-Cantano et al. (2019) showed a small impact of angular differences in homogeneous myocyte aggregate fields on global outputs, such as cavity volume, but a high influence of heterogeneity and local variations of myocyte aggregate orientation, when compared to homogeneous myocyte aggregate orientation fields on cavity volume and wall thickness. Eriksson et al. (2013) revealed a strong influence of heterogeneous microstructure on LV torsion. This highlights the benefits of personalized representations of the cardiac microstructure, despite the potential bias due to residual errors in the range of 10°. DTI measurements have become the most commonly used tool to non-destructively assess microstructure in organs. These measurements are suffering from low SNR and in the realm of e.g. in-vivo imaging a precision of 15.5° (systole)/31.9° (diastole) (Aliotta et al., 2018) was reported. Despite the data-induced error, its non-linear propagation and the reported mid-myocardium stiffening with increasing helix (Palit et al., 2015b), underlines the need for more realistic myocyte aggregate orientation representations, reducing the total model error. Error reduction in patient specific representations of myocyte aggregate orientation is therefore a prerequisite for image-based, patient-specific bio-mechanics modelling. The PGD and POD models are based on a functional

basis extracted form an ex-vivo DTI training data set, these basis functions describe common characteristics across the hearts, thus potentially suppressing noise in imaging data by truncation of the basis. The importance of a heterogeneous myocyte aggregate orientation (Rodríguez-Cantano et al., 2019; Eriksson et al., 2013) suggests that an atlas and the data-driven PGD and POD models have an advantage, compared to a global rule-based approach. Further, the PGD and POD model add natural variability along the circumferential and longitudinal coordinates.

A human show case was used to test the feasibility to transfer the PGD and POD model, using basis functions obtained from porcine data, to human aggregated myocyte orientation. The resulting ΔMA is in the same range as the results on the porcine data, suggesting the applicability of the porcine derived modes to human data. The PGD model uses the low-rank PGD basis averaged over the porcine training data set. This is personalized by fitting the SVD basis functions to the human data set. Without personalization (0 SVD modes), the error for the first PGD mode agrees well with the results for the porcine data. This suggests a good match of the first PGD mode, representing the most prominent global structural characteristics of the underlying human case. However, adding higher PGD modes without personalization worsens the median ΔMA, whereas it is improved or constant for the porcine data. Thus, the mean of those structural characteristics with increasing detail cannot be transferred directly from the porcine to human data. The devaition from the mean PGD mode, extracted from the porcine data set, to the human test case, could be compensated by a scaling factor for each 1D function of the mean PGD mode. If the same scaling factors could be used for other human test cases, remains an open question. For further investigation of the differences between the low-rank basis of porcine and human cardiac microstructure, an extraction of the model from human training data is feasible upon availability of ex-vivo human datasets. The poor approximation of the unpersonalized models, obtained from the porcine training data set (i.e. the mean PGD modes with 0 SVD modes, the porcine atlas and the RBM adapted to the porcine average data), indicates the interspecies difference. However, when using personalization with the SVD basis, extracted from the variations across the porcine training data, the PGD model approximation significantly improves with two PGD modes and 2 SVD modes already. This shows that it is possible to personalize the model to the underlying human data set using the basis functions of structural variations, extracted from porcine data. An error plateau is reached with 2 PGD and 4 SVD modes. This is no significant difference to the healthy porcine test cases, were the error levels off between 2 and 4 PGD modes with 4 SVD modes. For the POD model, only minor improvement is found when increasing the number of modes. The modes are not ordered by information content for the human data set. The POD model captures the main characteristic of the human show case. However, more detailed characteristics, represented by higher POD modes, are not dominant in the human show case. Both models can approximate the underlying human case, promising for the feasibility to transfer the models to human data. The un-personalized mean of the second and higher PGD modes can not be transferred to human data.

We performed a fit of the data-driven PGD and POD model to the 3D volumetric data to demonstrate that the derived low-rank basis functions represent aggregated myocyte orientation well. In personalized modelling, if no high-quality, high-resolution, 3D coverage DTI data is available, the PGD or POD model offers the potential to estimate a 3D representation of myocyte aggregate orientation on the mesh nodes form sparse data. The advantage of the models is the information transfer from high resolution data, while keeping the possibility for personalization. The functional bases give a realistic, globally heterogeneous prior. To fit the PGD model to data with low spatial coverage, a PGD of the sparse data set is required. Without changing the PGD method, the Galerkin basis functions need to be adapted to ensure that data points are available within the support of each Galerkin basis function. The new supporting points have to be a subset of the supporting points of the model. Subsequently, the weights of the PGD/SVD model can be adapted to fit the degrees of freedom to the target data in a least squares sense. Alternatively, the PGD could be adjusted, directly using the SVD basis and fitting the weights. To fit the POD model to sparse data, the data is mapped onto the closest grid points on the common grid, where the model is defined. A gappy POD (Willcox, 2006) could be used to fit the model parameters, using a linear least-squares method. Due to the choice of the 2D modes with transmural normal direction, data is available in each imaging slice. In clinical applications, slice miss-match is commonly found, due to breathing. The spatial miss-match of anatomical data and DTI data poses an additional task, when assigning the data points to the coordinates with respect to the LV geometry.

In future applications, when applying the model to a large cohort, a statistical analysis of the extracted weights could be used to obtain a realistic, high fidelity generative model of aggregated myocyte orientation representing natural variations. This might advance data augmentation for machine learning based studies, suffering from low data availability. Further, the correlation of weights could give insights in typical patterns present in cardiac microstructure. Or the weights could be used as a measure of global similarity between different data sets. Studies analyzing a potential change in weights in global disease involving remodelling, might reveal new biomarkers. The models and the basis functions, together with the set of weights and the original data are available at (https://doi.org/10.3929/ethz-b-000478084).

5. Conclusion

We have presented a new data-driven, volumetric, high-resolution, parametric model of LV myocyte orientation. We have demonstrated that aggregated myocyte orientation can be represented in a common low-rank basis in shape-adapted coordinates. The parametric model can be personalized to cDTI data and approximate unseen data. A personalized, heterogeneous field of aggregated myocytes results by transferring information about major structural characteristics and inter-case variability, from the ex-vivo training data. The human show case suggests the feasibility to transfer the model derived from porcine data to approximate human aggregated myocyte orientation.

Declaration of Competing Interest

The authors declare that they have no known competing financial interests or personal relationships that could have appeared to influence the work reported in this paper.

CRediT authorship contribution statement

Johanna Stimm: Conceptualization, Formal analysis, Investigation, Methodology, Software, Validation, Visualization, Writing - original draft. **Stefano Buoso:** Conceptualization, Formal analysis, Investigation, Methodology, Software, Validation, Writing - review & editing. **Ezgi Berberoğlu:** Methodology, Software, Writing - review & editing. **Sebastian Kozerke:** Funding acquisition, Resources, Software, Writing - review & editing. **Martin Genet:** Funding acquisition, Resources, Software, Writing - review & editing. **Christian T. Stoeck:** Conceptualization, Data curation, Funding acquisition, Methodology, Project administration, Validation, Resources, Supervision, Validation, Writing - review & editing.

Acknowledgements

This work has been supported by the Swiss National Science Foundation: PZ00P2_174144, CR23I3_166485 and the PHRT SWISS-HEART Failure Network (SHFN).

Supplementary material

Supplementary material associated with this article can be found, in the online version, at doi:10.1016/j.media.2021.102064

References

Aliotta, E., Moulin, K., Magrath, P., Ennis, D.B., 2018. Quantifying precision in cardiac diffusion tensor imaging with second-order motion-compensated convex optimized diffusion encoding. Magn. Reson. Med. 80 (3), 1074–1087. doi:10.1002/mrm.27107.

Bayer, J., Prassl, A.J., Pashaei, A., Gomez, J.F., Frontera, A., Neic, A., Plank, G., Vigmond, E.J., 2018. Universal ventricular coordinates: a generic framework for describing position within the heart and transferring data. Med. Image Anal. 45, 83–93. doi:10.1016/j.media.2018.01.005.

Bayer, J.D., Blake, R.C., Plank, G., Trayanova, N.A., 2012. A novel rule-based algorithm for assigning myocardial fiber orientation to computational heart models. Ann. Biomed. Eng. 40 (10), 2243–2254. doi:10.1007/s10439-012-0593-5.

Beyar, R., Sideman, S., 1984. A computer study of the left ventricular performance based on fiber structure, sarcomere dynamics, and transmural electrical propagation velocity.. Circ. Res. 55 (3), 358–375. doi:10.1161/01.RES.55.3.358.

Bovendeerd, P., Arts, T., Huyghe, J., van Campen, D., Reneman, R., 1992. Dependence of local left ventricular wall mechanics on myocardial fiber orientation: a model study. J. Biomech. 25 (10), 1129–1140. doi:10.1016/0021-9290(92)90069-D.

Buljak, V., Maier, G., 2011. Proper orthogonal decomposition and radial basis functions in material characterization based on instrumented indentation. Eng. Struct. 33 (2), 492–501. doi:10.1016/j.engstruct.2010.11.006.

Buoso, S., Manzoni, A., Alkadhi, H., Plass, A., Quarteroni, A., Kurtcuoglu, V., 2019. Reduced-order modeling of blood flow for noninvasive functional evaluation of coronary artery disease. Biomech. Model. Mechanobiol. 18 (6), 1867–1881. doi:10.1007/s10237-019-01182-w.

Canny, J., 2004. Lazy Snapping. In: 31st International Conference on Computer Graphics and Interactive Techniques.

Cerqueira, M.D., Weissman, N.J., Dilsizian, V., Jacobs, A.K., Kaul, S., Laskey, W.K., Pennell, D.J., Rumberger, J.A., Ryan, T., Verani, M.S., 2002. Standardized myocardial segmentation and nomenclature for tomographic imaging of the heart. Circulation 105 (4), 539–542. doi:10.1161/hc0402.102975.

Chinesta, F., Cueto, E., Huerta, A., 2014. PGD for solving multidimensional and parametric models. Separated Representations and PGD-Based Model Reduction. In: Chinesta, Francisco, Ladevèze, Pierre (Eds.). CISM International Centre for Mechanical Sciences, 554. Springer Vienna, Vienna doi:10.1007/978-3-7091-1794-1_2.

Chinesta, F., Keunings, R., Leygue, A., 2014. The Proper Generalized Decomposition for Advanced Numerical Simulations. Springer Briefs in Applied Sciences and Technology. Springer International Publishing, Cham doi:10.1007/978-3-319-02865-1.

Doste, R., Soto-Iglesias, D., Bernardino, G., Alcaine, A., Sebastian, R., Giffard-Roisin, S., Sermesant, M., Berruezo, A., Sanchez-Quintana, D., Camara, O., 2019. A rule-based method to model myocardial fiber orientation in cardiac biventricular geometries with outflow tracts. Int. J. Numer. Methods Biomed. Eng. 35 (4), e3185. doi:10.1002/cnm.3185.

Eriksson, T., Prassl, A., Plank, G., Holzapfel, G., 2013. Influence of myocardial fiber/sheet orientations on left ventricular mechanical contraction. Math. Mech. Solids 18 (6), 592–606. doi:10.1177/1081286513485779.

Firbank, M.J., Coulthard, A., Harrison, R.M., Williams, E.D., 1999. A comparison of two methods for measuring the signal to noise ratio on MR images. Phys. Med. Biol. 44 (12), N261–N264. doi:10.1088/0031-9155/44/12/403.

Geerts, L., Kerckhoffs, R., Bovendeerd, P., Arts, T., 2003. Towards patient specific models of cardiac mechanics: a sensitivity study. In: Lecture Notes in Computer Science (including subseries Lecture Notes in Artificial Intelligence and Lecture Notes in Bioinformatics), 2674, pp. 81–90. doi:10.1007/3-540-44883-7_9.

Genet, M., Rausch, M.K., Lee, L.C., Choy, S., Zhao, X., Kassab, G.S., Kozerke, S., Guccione, J.M., Kuhl, E., 2015. Heterogeneous growth-induced prestrain in the heart. J. Biomech. 48 (10), 2080–2089. doi:10.1016/j.jbiomech.2015.03.012.

Genet, M., Von Deuster, C., Stoeck, C.T., Kozerke, S., 2015. 3D myofiber reconstruction from in vivo cardiac DTI data through extraction of low rank modes. ISMRM 23rd Annual Meeting and Exhibition 2015. MRM, Toronto, Canada.

Gilbert, S.H., Benson, A.P., Li, P., Holden, A.V., 2007. Regional localisation of left ventricular sheet structure: integration with current models of cardiac fibre, sheet and band structure. Eur. J. Cardio-Thoracic Surg. 32 (2), 231–249. doi:10.1016/j.ejcts.2007.03.032.

Healy, L.J., Jiang, Y., Hsu, E.W., 2011. Quantitative comparison of myocardial fiber structure between mice, rabbit, and sheep using diffusion tensor cardiovascular magnetic resonance. J. Cardiovasc. Magn. Reson. 13 (1), 74. doi:10.1186/1532-429X-13-74.

Karadag, I.E., Bishop, M., Hales, P.W., Schneider, J.E., Kohl, P., Gavaghan, D., Grau, V., 2011. Regionally optimised mathematical models of cardiac myocyte orientation in rat hearts. In: Metaxas D.N., A.L. (Ed.), Functional Imaging and Modeling of the Heart. FIMH 2011. Lecture Notes in Computer Science.. Springer Berlin Heidelberg, pp. 294–301. doi:10.1007/978-3-642-21028-0_36.

LeGrice, I.J., Hunter, P.J., Smaill, B.H., 1997. Laminar structure of the heart: a mathematical model. Am. J. Physiology-Heart Circ. Physiol. 272 (5), H2466–H2476. doi:10.1152/ajpheart.1997.272.5.H2466.

Lekadir, K., Hoogendoorn, C., Pereanez, M., Alba, X., Pashaei, A., Frangi, A.F., 2014. Statistical personalization of ventricular fiber orientation using shape predictors. IEEE Trans. Med. Imaging 33 (4), 882–890. doi:10.1109/TMI.2013.2297333.

Lim, J.S., 1990. Two-Dimensional Signal and Image Processing. Prentice Hall, Englewood Cliffs, NJ, p. 710.

Lombaert, H., Peyrat, J., Croisille, P., Rapacchi, S., Fanton, L., Cheriet, F., Clarysse, P., Magnin, I., Delingette, H., Ayache, N., 2012. Human atlas of the cardiac fiber architecture: study on a healthy population. IEEE Trans. Med. Imaging 31 (7), 1436–1447. doi:10.1109/TMI.2012.2192743.

Lombaert, H., Peyrat, J.-M., Croisille, P., Rapacchi, S., Fanton, L., Clarysse, P., Delingette, H., Ayache, N., 2011. Statistical analysis of the human cardiac fiber architecture from DT-MRI. In: Functional Imaging and Modeling of the Heart. FIMH 2011. Lecture Notes in Computer Science., 19. Springer, Berlin, Heidelberg, pp. 171–179. doi:10.1007/978-3-642-21028-0_22.

Lunkenheimer, P.P., Niederer, P., 2012. Hierarchy and inhomogeneity in the systematic structure of the mammalian myocardium: towards a comprehensive view of cardiodynamics. Technol. Health Care 20 (5), 423–434. doi:10.3233/THC-2012-0690.

Mekkaoui, C., Jackowski, M.P., Kostis, W.J., Stoeck, C.T., Thiagalingam, A., Reese, T.G., Reddy, V.Y., Ruskin, J.N., Kozerke, S., Sosnovik, D.E., 2018. Myocardial scar delineation using diffusion tensor magnetic resonance tractography. J. Am. Heart Assoc. 7 (3). doi:10.1161/JAHA.117.007834.

Mojica, M., Pop, M., Sermesant, M., Ebrahimi, M., 2020. Novel atlas of fiber directions built from ex-vivo diffusion tensor images of porcine hearts. Comput. Methods Prog. Biomed. 187, 105200. doi:10.1016/j.cmpb.2019.105200.

Murphy, B., Carson, P., Ellis, J., Zhang, Y., Hyde, R., Chenevert, T., 1993. Signal-to-noise measures for magnetic resonance imagers. Magn. Reson. Imaging 11 (3), 425–428. doi:10.1016/0730-725X(93)90076-P.

Nagler, A., Bertoglio, C., Gee, M., Wall, W., 2013. Personalization of cardiac fiber orientations from image data using the unscented Kalman filter. In: Ourselin, S., Rueckert, D., Smith, N. (Eds.), Functional Imaging and Modeling of the Heart. FIMH 2013. Lecture Notes in Computer Science. Springer, Berlin, Heidelberg, pp. 132–140. doi:10.1007/978-3-642-38899-6_16.

Nagler, A., Bertoglio, C., Ortiz, M., Wall, W., Wall, W.A., 2016. A spatially Varying Mathematical Representation of the Biventricular Cardiac Fiber Architecture. Technical Report. Institute for Computational Mechanics, Technische Universität München; Center for Mathematical Modeling, Universidad de Chile..

Nikou, A., Dorsey, S.M., McGarvey, J.R., Gorman, J.H., Burdick, J.A., Pilla, J.J., Gorman, R.C., Wenk, J.F., 2016. Computational modeling of healthy myocardium in diastole. Ann. Biomed. Eng. 44 (4), 980–992. doi:10.1007/s10439-015-1403-7.

Nikou, A., Dorsey, S.M., McGarvey, J.R., Gorman, J.H., Burdick, J.A., Pilla, J.J., Gorman, R.C., Wenk, J.F., 2016. Effects of using the unloaded configuration in predicting the in vivo diastolic properties of the heart. Comput. Methods Biomech. Biomed. Eng. 19 (16), 1714–1720. doi:10.1080/10255842.2016.1183122.

Palit, A., Bhudia, S.K., Arvanitis, T.N., Turley, G.A., Williams, M.A., 2015. Computational modelling of left-ventricular diastolic mechanics: effect of fibre orientation and right-ventricle topology. J. Biomech. 48 (4), 604–612. doi:10.1016/j.jbiomech.2014.12.054.

Palit, A., Bhudia, S.K., Arvanitis, T.N., Turley, G.A., Williams, M.A., 2015. Computational modelling of left-ventricular diastolic mechanics: effect of fibre orientation and right-ventricle topology. J. Biomech. 48 (4), 604–612. doi:10.1016/j.jbiomech.2014.12.054.

Parker, J.R., 2010. Algorithms for Image Processing and Computer Vision. Wiley Publishing, Inc., Indianapolis, Indiana.

Paun, B., Bijnens, B., Iles, T., Iaizzo, P.A., Butakoff, C., 2017. Patient independent representation of the detailed cardiac ventricular anatomy. Med. Image Anal. 35, 270–287. doi:10.1016/j.media.2016.07.006.

Peyrat, J.-M., Sermesant, M., Pennec, X., Delingette, H., Chenyang Xu, McVeigh, E., Ayache, N., 2007. A computational framework for the statistical analysis of cardiac diffusion tensors: application to a small database of canine hearts. IEEE Trans. Med. Imaging 26 (11), 1500–1514. doi:10.1109/TMI.2007.907286.

Piuze, E., Lombaert, H., Sporring, J., Strijkers, G.J., Bakermans, A.J., Siddiqi, K., 2013. Atlases of cardiac fiber differential geometry. In: International Conference on Functional Imaging and Modeling of the Heart 2013. Springer, Berlin, Heidelberg, pp. 442–449. doi:10.1007/978-3-642-38899-6_52.

Pluijmert, M., Delhaas, T., de la Parra, A.F., Kroon, W., Prinzen, F.W., Bovendeerd, P.H.M., 2017. Determinants of biventricular cardiac function: a mathematical model study on geometry and myofiber orientation. Biomech. Model. Mechanobiol. 16 (2), 721–729. doi:10.1007/s10237-016-0825-y.

Potse, M., Dube, B., Richer, J., Vinet, A., Gulrajani, R., 2006. A comparison of monodomain and bidomain reaction-diffusion models for action potential propagation in the human heart. IEEE Trans. Biomed. Eng. 53 (12), 2425–2435. doi:10.1109/TBME.2006.880875.

Rodríguez-Cantano, R., Sundnes, J., Rognes, M.E., 2019. Uncertainty in cardiac myofiber orientation and stiffnesses dominate the variability of left ventricle deformation response. Int. J. Numer. Methods Biomed. Eng. 35 (5), e3178. doi:10.1002/cnm.3178.

Rossi, S., Lassila, T., Ruiz-Baier, R., Sequeira, A., Quarteroni, A., 2014. Thermodynamically consistent orthotropic activation model capturing ventricular systolic wall thickening in cardiac electromechanics. Eur. J. Mech. A/Solids 48 (1). doi:10.1016/j.euromechsol.2013.10.009.

Sack, K.L., Aliotta, E., Ennis, D.B., Choy, J.S., Kassab, G.S., Guccione, J.M., Franz, T., 2018. Construction and validation of subject-specific biventricular finite-element models of healthy and failing swine hearts from high-resolution DT-MRI. Front. Physiol. 9 (MAY). doi:10.3389/fphys.2018.00539.

Scollan, D.F., Holmes, A., Winslow, R., Forder, J., 1998. Histological validation of myocardial microstructure obtained from diffusion tensor magnetic resonance imaging. Am. J. Physiology-Heart Circ. Physiol. 275 (6), H2308–H2318. doi:10.1152/ajpheart.1998.275.6.H2308.

Sosnovik, D.E., Mekkaoui, C., Huang, S., Chen, H.H., Dai, G., Stoeck, C.T., Ngoy, S., Guan, J., Wang, R., Kostis, W.J., Jackowski, M.P., Wedeen, V.J., Kozerke, S., Liao, R., 2014. Microstructural impact of ischemia and bone Marrow–Derived cell therapy revealed with diffusion tensor magnetic resonance imaging tractography of the heart in vivo. Circulation 129 (17), 1731–1741. doi:10.1161/CIRCULATIONAHA.113.005841.

Sosnovik, D.E., Wang, R., Dai, G., Wang, T., Aikawa, E., Novikov, M., Rosenzweig, A., Gilbert, R.J., Wedeen, V.J., 2009. Diffusion spectrum MRI tractography reveals the presence of a complex network of residual myofibers in infarcted myocardium. Circulation 2 (3), 206–212. doi:10.1161/CIRCIMAGING.108.815050.

Stoeck, C.T., von Deuster, C., Fleischmann, T., Lipiski, M., Cesarovic, N., Kozerke, S., 2018. Direct comparison of in vivo versus postmortem second-order motion-compensated cardiac diffusion tensor imaging. Magn. Reson. Med. 79 (4), 2265–2276. doi:10.1002/mrm.26871.

Streeter, D.D., Spotnitz, H.M., Patel, D.P., Ross, J., Sonnenblick, E.H., 1969. Fiber orientation in the canine left ventricle during diastole and systole. Circ. Res. 24 (3), 339–347. doi:10.1161/01.RES.24.3.339.

Toussaint, N., Sermesant, M., Stoeck, C.T., Kozerke, S., Batchelor, P.G., 2010. In vivo human 3D cardiac fibre architecture: reconstruction using curvilinear interpolation of diffusion tensor images. In: Jiang, T. (Ed.), MICCAI 2010. Lecture Notes in Computer Science.. In: LNCS, 6361. Springer Berlin Heidelberg, pp. 418–425. doi:10.1007/978-3-642-15705-9_51.

Toussaint, N., Stoeck, C.T., Schaeffter, T., Kozerke, S., Sermesant, M., Batchelor, P.G., 2013. In vivo human cardiac fibre architecture estimation using shape-based diffusion tensor processing. Med. Image Anal. 17 (8), 1243–1255. doi:10.1016/j.media.2013.02.008.

Vadakkumpadan, F., Arevalo, H., Ceritoglu, C., Miller, M., Trayanova, N., 2012. Image-based estimation of ventricular fiber orientations for personalized modeling of cardiac electrophysiology. IEEE Trans. Med. Imaging 31 (5), 1051–1060. doi:10.1109/TMI.2012.2184799.

Wang, V.Y., Casta, C., Zhu, Y.-M., Cowan, B.R., Croisille, P., Young, A.A., Clarysse, P., Nash, M.P., 2016. Image-based investigation of human in vivo myofibre strain. IEEE Trans. Med. Imaging 35 (11), 2486–2496. doi:10.1109/TMI.2016.2580573.

Willcox, K., 2006. Unsteady flow sensing and estimation via the gappy proper orthogonal decomposition. Comput. Fluids 35 (2), 208–226. doi:10.1016/j.compfluid.2004.11.006.

Wong, J., Kuhl, E., 2014. Generating fibre orientation maps in human heart models using Poisson interpolation. Comput. Methods Biomech. Biomed. Eng. 17 (11), 1217–1226. doi:10.1080/10255842.2012.739167.

Zhang, Y., Wei, H., 2017. Atlas construction of cardiac fiber architecture using a multimodal registration approach. Neurocomputing 259, 219–225. doi:10.1016/j.neucom.2016.08.125.